Impact of divertor plasma parameters on characteristics of current-convective turbulence under DIII-D-like detached conditions

Cite as: Phys. Plasmas **26**, 122303 (2019); https://doi.org/10.1063/1.5123388
Submitted: 05 August 2019 . Accepted: 04 November 2019 . Published Online: 06 December 2019

A. A. Stepanenko, H. Q. Wang, and S. I. Krasheninnikov

Physics of Plasmas ARTICLE scitation.org/journal/php

Impact of divertor plasma parameters on characteristics of current-convective turbulence under DIII-D-like detached conditions

Cite as: Phys. Plasmas **26**, 122303 (2019); doi: 10.1063/1.5123388
Submitted: 5 August 2019 · Accepted: 4 November 2019 ·
Published Online: 6 December 2019

A. A. Stepanenko,[1,a)] H. Q. Wang,[2] and S. I. Krasheninnikov[3]

AFFILIATIONS

[1]National Research Nuclear University MEPhI (Moscow Engineering Physics Institute), Kashirskoe Highway, 31, 115409 Moscow, Russia
[2]General Atomics, PO Box 85608, San Diego, California 92186-5608, USA
[3]Department of Mechanical and Aerospace Engineering, University of California San Diego, 9500 Gilman Drive, La Jolla, California 92093, USA

[a)]Electronic mail: aastepanenko@mephi.ru

ABSTRACT

Recent observations of turbulence in plasma of a DIII-D inner divertor revealed the formation of poloidally localized fluctuations with frequencies in the low-kilohertz range, when the machine was operating in the fluctuating state of detachment. This phenomenon can be related to the onset of the current-convective instability (CCI). In this contribution, we use the basic physical model of the instability to simulate the saturated current-convective turbulence under the DIII-D-like detached conditions. Parameter scans of turbulence characteristics are performed. The spatial and temporal spectra of fluctuations are obtained and compared with the available experimental data. It is demonstrated that simulations are able to qualitatively reproduce most of the distinct features of turbulence found in the experiments, indicating that the CCI can be a plausible mechanism responsible for plasma activity recently observed in DIII-D.

I. INTRODUCTION

Plasma detachment is the crucial element in strategies sought for mitigating extreme heat and particle loads to the first wall envisaged in modern tokamaks and future tokamak-reactors.[1–3] The physics of detachment is multifaceted[4,5] and involves a vast number of processes, including highly nonlinear phenomena, such as bifurcations of plasma equilibrium[6,7] and turbulence.[8,9] Turbulence plays a dual role with the classical collisional transport in governing energy and mass fluxes coming to the plasma facing components in the machine, thus determining their lifespan.

Experimental observations[10–16] and existing theoretical models of instabilities[9,17–20] driving turbulence in detached divertor plasma have established a solid basis for the understanding of the transport processes in the tokamak edge. Nevertheless, there still remain physical phenomena, whose mechanisms are not yet thoroughly understood.[4]

Measurements of plasma radiation intensity in the inner divertor of ASDEX Upgrade (AUG)[15] have demonstrated the onset of strong fluctuations in the vicinity of the X-point, with amplitudes reaching 12%–15% of the equilibrium radiation signal and with frequencies in the low-kilohertz (1–10 kHz) range. This turbulence appeared when plasma was in the so-called fluctuating state of detachment, characterized by strong temperature asymmetry between the divertors. Similar fluctuations were also reported for DIII-D by Wang *et al.*[21] In that study, oscillations of the magnetic field and plasma current were observed at the target plates in the inner divertor leg of the machine, when it was operating under the detachment conditions, similar to the AUG fluctuating state. Herein, the spectrograms of oscillations were dominated by low-kilohertz components, akin to spectra of radiation fluctuations found at AUG.

One of the possible mechanisms for the onset of turbulence with such characteristics is the current-convective instability (CCI).[22] The first analytical estimates of the CCI growth rate have confirmed its plausibility for ASDEX Upgrade.[22] Later on, the first simulations of the current-convective turbulence (CCT) in the AUG-like setup have supported that conclusion.[23] Modeling of the CCT under the DIII-D-like detached conditions[24] have yielded spatial and temporal spectra of turbulence similar to those found in experiments.[21] Nevertheless, the simulations also revealed discrepancies between the experimental

data and theoretical predictions.[23,24] For this reason, more work is still needed to fully verify whether the CCI can lead to turbulence observed in AUG and DIII-D and, possibly, in other machines.

In this paper, we continue to analyze the properties of CCT under the DIII-D-like detachment conditions and consider the impact of edge plasma parameters on the spatial and temporal structure of the saturated turbulence. The rest of this paper is organized as follows. In Sec. II, we briefly summarize the DIII-D experimental results, important for our work. Section III covers the details of the CCI physical model and parameters of plasma and magnetic geometry employed for simulations. The results of modeling are presented and analyzed in Sec. IV. Discussion of the results and conclusions is given in Sec. V.

II. EXPERIMENTAL DATA

Before going into the details of the CCT simulations, we summarize the main turbulence features observed in DIII-D experiments with detached plasmas.[21]

Experimental data were gathered by using the Langmuir probes and magnetic sensors placed across the inner and outer divertor legs of the machine. As a result, signals of the parallel current, ion flux, and poloidal magnetic field oscillations were available for the reconstruction of the temporal and spatial spectra of plasma fluctuations. In what follows, we will not consider perturbations of the ion flux and poloidal magnetic field due to the limitations of the CCI physical model, used for simulations. Instead, only oscillations of the parallel current $\delta j_\parallel$ will be of interest. For this reason and since the ion flux and magnetic field signals are closely related to $\delta j_\parallel$, below we will focus on peculiarities of the current oscillations, found in experiments:

1. Frequency spectra of saturated fluctuations $P(f)$ show the presence of several dominant components with frequencies lying in the low-kilohertz (low-f) range, on the order of $f \sim 1 - 10$ kHz.
2. Spatial spectra of perturbations, $S(\mathbf{k})$ ($\mathbf{k}$ is the wave vector), measured at different poloidal locations across the inner divertor leg, demonstrate that (i) the fluctuations are localized in the poloidal direction and (ii) in the toroidal direction, they are dominated by large-scale modes, having the toroidal mode numbers $n_\zeta = 1, 2$.
3. Amplitudes of signals $\delta j_\parallel$ can be comparable to the values of the background current, $j_\parallel$, $\delta j_\parallel / j_\parallel \sim 1$.

These observations are the basis for the further analysis of plasma dynamics driven by the current-convective instability.

III. CCI PHYSICAL MODEL

A. Governing equations

To simulate the current-convective turbulence, we employ the CCI physical model, used in Refs. 23 and 24 for initial simulations of divertor plasma turbulence under AUG- and DIII-D-like detached conditions. The details of the model (in particular, the set of physical approximations and analysis of its applicability for divertor plasma) can be found in Ref. 23. The main governing dynamical equations describe evolution of the plasma vorticity, $\varpi = \nabla_\perp^2 \varphi$, and electron temperature, T_e,

$$\left(\frac{\partial}{\partial t} + \mathbf{V}_{\mathrm{E}\times\mathrm{B}} \cdot \nabla\right) \varpi = 4\pi \frac{v_A^2}{c^2} \nabla_\parallel j_\parallel, \tag{1}$$

$$\frac{3}{2} n_0 \left(\frac{\partial}{\partial t} + \mathbf{V}_{\mathrm{E}\times\mathrm{B}} \cdot \nabla\right) T_e + \nabla_\parallel q_{e\parallel} = 0. \tag{2}$$

Here, $j_\parallel = -\sigma \partial_\parallel [\varphi - 1.71(T_e/e)]$ is the parallel plasma current, $q_{e\parallel} = -\varkappa_{e\parallel} \partial_\parallel T_e$ is the diffusive parallel electron heat flux, φ is the electrostatic potential, $\sigma = 1.96 n_0 e^2/(\nu_{ei} m_e)$ is the parallel electric conductivity, $\varkappa_{e\parallel} = 3.16 n_0 T_e/(\nu_{ei} m_e)$ is the parallel electron thermal conductivity, $\nu_{ei} = 4\sqrt{2\pi} n_0 e^4 \ln\Lambda_{ei}/(3 m_e^{1/2} T_e^{3/2})$ is the electron-ion collision frequency, $n_0 = \mathrm{const}$ is the background plasma density, $\mathbf{V}_{\mathrm{E}\times\mathrm{B}} = (c/B^2)\mathbf{B} \times \nabla\varphi$ is the plasma advection velocity in crossed electric and magnetic fields, $v_A = B/\sqrt{4\pi m_i n_0}$ is the Alfvén velocity, c is the light speed, m_e and m_i are the electron and ion masses, respectively, and e is the elementary charge. Equations (1) and (2) are a subset of the full seven-field system of drift-ordered two-fluid MHD equations of Ref. 25.

We emphasize that the CCI physical model, used in this work, incorporates only a minimum set of physical mechanisms necessary to initiate and suppress the instability.[23,24] In doing so, we aim at analyzing whether a series of turbulence features found in experiments (see Sec. II) can be reproduced using this simulation model of the instability.

The physical mechanisms, which have been omitted from consideration, include, among others, the presence of neutral particles. The neutrals are abundant in detached conditions and, strictly speaking, have to be taken into account when modeling dynamics of divertor plasmas. However, in the limit of a stationary background, neutrals would mainly act as the energy sink for the instability, suppressing its dynamics and thus merely lowering the frequencies and amplitudes of the unstable modes. In this case, it can be anticipated that the simulation results would be qualitatively the same, as in the case with no neutrals. In the opposite situation, when neutrals are coevolved with plasma, a broader number of instabilities, including MARFEs,[17] ionization front jumps,[18] etc.,[24] would emerge, hindering the analysis of the CCT characteristics. As a result, in what follows the effects of neutral particles on dynamics of divertor plasma will be fully neglected.

The CCI dynamics will be analyzed in the simplified sheared slab geometry with the magnetic field strength kept constant in the whole simulation domain, $B = \mathrm{const}$. Although this geometry is less accurate than, e.g., the quasiballooning or toroidal coordinate systems,[26,27] it allows a more flexible definition of the magnetic field parameters, such as the shear, L_s, and connection, $L_\parallel$, lengths. Figures 1 and 2 show the sketches of the employed reference system and the general magnetic geometry of the machine, respectively. As seen in Fig. 2, the employed coordinate system is the rectified counterpart of the tokamak magnetic geometry in the inner divertor leg. The x axis of the reference system is directed normal to the magnetic flux surfaces ψ. It spans the space between the radial walls of the leg covering the distance Δ_x. The y axis follows the magnetic field lines. At $x = 0$, this axis is oriented along a reference field line $\mathbf{B}_0$. The y coordinate is measured from the divertor target plates up to the X-point region, which will be termed "upstream" further on. This notation is not to be confused with the actual upstream region of tokamaks. In this study, it merely refers to the upper segment of the divertor leg, to which the simulation domain is constrained. The connection length between the target plate and the X-point, measured along the magnetic field lines, is denoted as $L_\parallel$. The z axis is aligned orthogonal to both the x axis and the vector $\mathbf{B}_0$ and imitates the toroidal axis ζ of the machine (see Figs. 1 and 2). The size of the simulation domain in the z direction, Δ_z, is defined so that its projection onto the toroidal axis of the machine would yield the complete circumference of the tokamak inside the inner divertor leg, $\Delta_\zeta = 2\pi R$ (R is the local major radius). In other words, $\Delta_z = \Delta_\zeta (B_p/B)$.

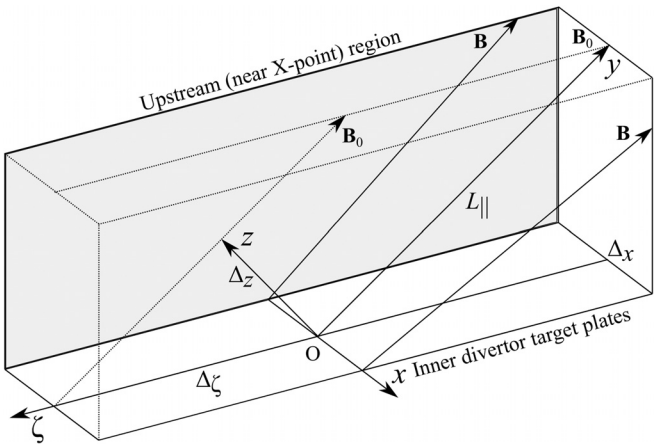

FIG. 1. The sketch of the magnetic geometry for the sheared slab coordinate system.

Equations (1) and (2) are supplied with the set of model boundary conditions.[23,24] In the z direction, all quantities satisfy the periodic boundary condition, $F(z=0) = F(z=\Delta_z)$ (F is an arbitrary scalar/vector field). At the radial, x, boundaries of the simulation domain, the zero-gradient boundary conditions are imposed on plasma variables, $\partial F/\partial x|_{x=0,\Delta_x} = 0$. Along the magnetic field lines, we use the following conditions:

$$\varphi|_{y=0} = 0, \quad \varphi|_{y=L_\parallel} = \varphi_u(x), \tag{3}$$

$$T_e|_{y=0} = T_t(x), \quad T_e|_{y=L_\parallel} = T_u(x). \tag{4}$$

In these relations, T_t is the electron temperature at the divertor target plate and T_u and φ_u are the electron temperature and the plasma potential at the upper end of the magnetic field line (upstream region), respectively. The quantities T_t, T_u, and φ_u are defined with the model profiles

$$T_t(x) = T_0, \tag{5}$$

$$T_u(x) = T_0 + T_m \exp\left[-(x/\delta_T)^2\right], \tag{6}$$

$$\varphi_u(x) = \varphi_m \exp\left[-(x/\delta_\varphi)^2\right], \tag{7}$$

imitating the actual distributions of the electron temperature and plasma potential at the entrance into the inner divertor leg and at the target plate. In these relations, $T_0 = \text{const}$ is the background electron temperature, T_m and φ_m are constants, and δ_T and δ_φ are the characteristic decay lengths. Since φ_u is the electrostatic potential in plasma, the parameters T_m and φ_m are connected to each other through the relation $\varphi_m = 3(T_m/e)$.

The initial distributions of the evolving variables, ϖ, φ, and T_e, are the steady-state solutions of Eqs. (1) and (2) matched with the boundary conditions (3) and (4),[23,24]

$$T_{e0}(x,y) = \left[T_t^{7/2} + (y/L_\parallel)\left(T_u^{7/2} - T_t^{7/2}\right)\right]^{2/7}, \tag{8}$$

$$\varphi_0(x,y) = 1.71\frac{T_{e0} - T_t}{e} + \left(\varphi_u - 1.71\frac{T_u - T_t}{e}\right)\frac{T_{e0}^2 - T_t^2}{T_u^2 - T_t^2}, \tag{9}$$

$$\varpi_0(x,y) = \nabla_\perp^2 \varphi_0(x,y). \tag{10}$$

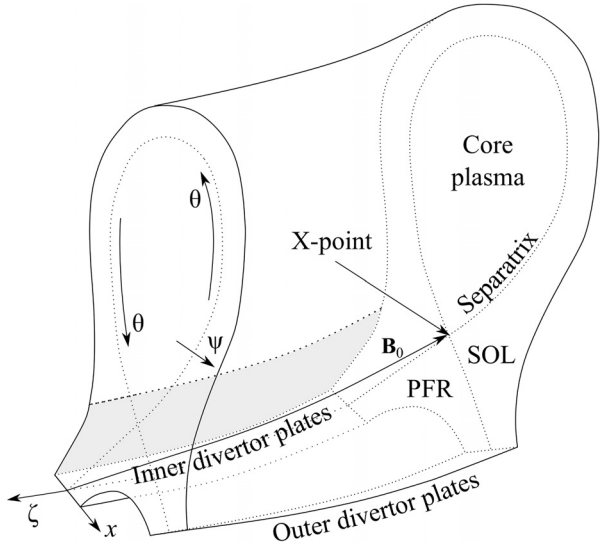

FIG. 2. The sketch of the magnetic field geometry in a tokamak. Reprint with permission from A. Stepanenko and H. Q. Wang, Plasma Phys. Rep. **45**, 627 (2019). Copyright 2019 Pleiades Publishing, Ltd.[24]

B. Simulation parameters

For simulations of CCI dynamics, we used the set of magnetic field parameters analogous to the experimental ones.[21] The connection and shear lengths were set to $L_\parallel = 14\,\text{m}$ and $L_s = 0.5\,\text{m}$, respectively. The size of the domain in the x direction was $\Delta_x = 20\,\text{cm}$. As mentioned above, the scale Δ_z was chosen to reproduce the effective toroidal size of the simulation domain on the order of the DIII-D circumference inside the inner divertor leg. Given the major radius coordinate $R \approx 1.1\,\text{m}$, we obtain $\Delta_\zeta \equiv 2\pi R = \Delta_z(B/B_p) \approx 6.9\,\text{m}$. The toroidal, B_t, and poloidal, B_p, magnetic field strengths were set to $B_t = 1.8\,\text{T}$ and $B_p = 0.02\,\text{T}$, yielding $\Delta_z = 7.7\,\text{cm}$.

The plasma parameters used for simulations were varied between modeling cases, and for this reason, they are covered in appropriate sections below. The only plasma parameters that were the same for all simulation cases were the background electron temperature and plasma density, $T_0 = 5\,\text{eV}$, $n_0 = 5.4 \times 10^{19}\,\text{m}^{-3}$, and the transverse scales δ_T and δ_φ, which were set to $\delta_T = \delta_\varphi = \delta = 3\,\text{cm}$. The chosen parameters approximately correspond to those found in experiments.[21]

The above values of plasma and magnetic field parameters are somewhat different from those used in Ref. 24. Apart from considering CCT dynamics in a separate (yet physically analogous) simulation setup, this choice allowed us to analyze what turbulence features would persist between alternative modeling cases. Both sets of parameters (used in the present work and in Ref. 24) are briefly summarized in Table I.

For modeling, we used the code written in the BOUT++ framework.[28] The space discretization of the differential operators was performed with a combination of the 4th-order central differencing/3rd-order WENO schemes for regular/upwind derivatives. The time

TABLE I. Parameters of plasma and magnetic fields used for CCT simulations.

Parameter	This work	Ref. 24
$L_\parallel$, m	14	20
L_s, m	0.5	0.6
B_t, T	1.8	2.0
B_p, T	0.020	0.036
Δ_z, cm	7.7	12.4
Δ_x, cm	20	10
δ, cm	3	2
T_0, eV	5	5
n_0, 10^{19} m^{-3}	5.4	4.0

integration was performed with the CVODE solver from the SUNDIALS suite.[29] The stability and convergence of the numerical scheme were successfully tested in Ref. 23. The code was supplied with grids with the resolution of $N_x \times N_y \times N_z = 260 \times 15 \times 257$ in the x, y, and z directions, respectively. The chosen number of grid points was sufficient to resolve the CCT spatial structure.[24]

IV. SIMULATION RESULTS

A. Methodology of obtaining turbulence spectra

To analyze spatial and temporal spectra of the current-convective turbulence, we used techniques previously described and discussed in Refs. 23 and 24.

To probe the frequency composition of saturated fluctuations, the values of the parallel current and electron temperature were sampled at several fixed points across the simulation domain. Three of them were located in plasma bulk, and the fourth one was placed at the boundary of the domain, approximately at the location of the inner strike point (ISP) in a real machine. Positions of the reference points are shown in Fig. 3, along with the contour lines of the initial electron temperature profile.

Frequency spectra were reconstructed using the oscillating parts of the signals, $\delta F(t) = F(\mathbf{r}, t) - \mathbb{E}[F(\mathbf{r}, t)]$ ($F = j_\parallel$, T_e and $\mathbb{E}[F(\mathbf{r}, t)]$ is the expected value of F at the location $\mathbf{r}$), measured when the saturated turbulent state of plasma dynamics was achieved. Then, a sampled time series $\delta F(t)$ was divided into equal subseries each having 2500 sample points. Afterward, the Fourier transform was applied to the subseries and the resulting spectra were averaged to produce the final power spectrum of turbulence.

For analysis of frequency spectra, we sampled 10 000 points in each simulation run, except for the run with $\max(T_u) = 65$ eV (this one is covered in Sec. IV C 1 and shown in Table II). For that case, we sampled 5000 points since the chosen value of T_u was way greater than the experimental values,[21,30] and for this reason, it was chosen to test the response of the turbulence characteristics to large values of the electron temperature.

Spatial spectra of turbulence were obtained by using data on electron temperature fluctuations in the vicinity of the divertor target plate. For analysis, the Fourier transform along the z direction was applied to the signals $\delta T_e(x, 0, z, t) = T_e(x, 0, z, t) - T_e(x, 0, z, 0)$ to finally arrive at spectra $|\delta \hat{T}_e(x, 0, k_z, t)|$. To ease the comparison of these quantities with data from Ref. 24, values of $|\delta \hat{T}_e(x, 0, k_z, t)|$ were additionally normalized to unity.

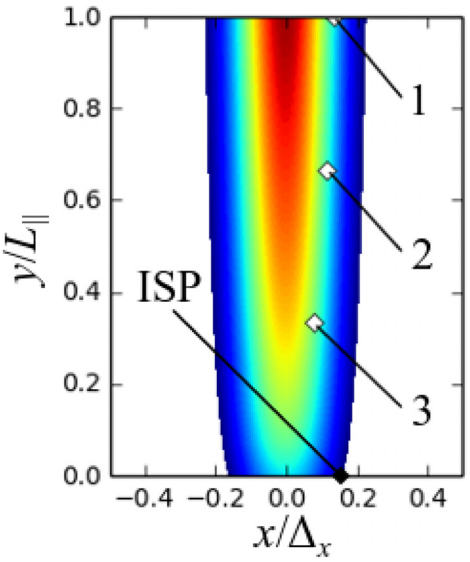

FIG. 3. Positions of the fixed points for probing plasma parameters. The contour lines qualitatively represent the initial distribution of the electron temperature in the simulation domain.

B. Spatial-temporal spectra of saturated current-convective turbulence

Figure 4 demonstrates the spatial dynamics of the electron temperature fluctuations in case, when the maximum upstream electron temperature was equal to 25 eV. Panels (a) and (b) of the figure show examples of the electron temperature distributions in the z direction, obtained in the near-target region of the domain at the moments of time, corresponding to the linear and saturated nonlinear stages of the instability. Both states were identified analogous to Ref. 24.

Figure 5 demonstrates the spatial spectra of the T_e fluctuations in the near target region in the linear and nonlinear phases of the instability. As seen in panel (a) of Fig. 5, the linear stage of the instability is characterized by a large wave number of $k_z \approx 24\,\mathrm{cm}^{-1}$, corresponding to the mode number of $n_z \approx 28$. Thus, the linear stage of the CCI is dominated by small-scale fluctuations in the toroidal direction. As the transition to saturated turbulence occurs, Fig. 5, panel (b), the structure of the T_e fluctuations in the z direction changes and small-scale oscillations give way to the large scale ones, characterized by small wave numbers $k_z \approx 1, 2\,\mathrm{cm}^{-1}$, corresponding to the mode numbers $n_z = 1, 2$. These results completely agree with the experimental observations,[21]

TABLE II. Parameters of the parallel current fluctuations, measured at the inner strike point, for the upstream electron temperature scan.

$\max(T_u)$, eV	f, kHz[a]	$S[\delta j_\parallel]$, A/cm^2	$\mathbb{E}[j_\parallel]$, A/cm^2
15	2.8	1.0	8.8
25	5.9	2.1	26.1
35	10.0	3.3	54.9
65	14.2	7.8	236.0

[a]The frequency of the dominant mode was found as the center-of-mass of the power spectrum with values below the threshold level, $P/P_{\max} < 0.4$, set to zero.

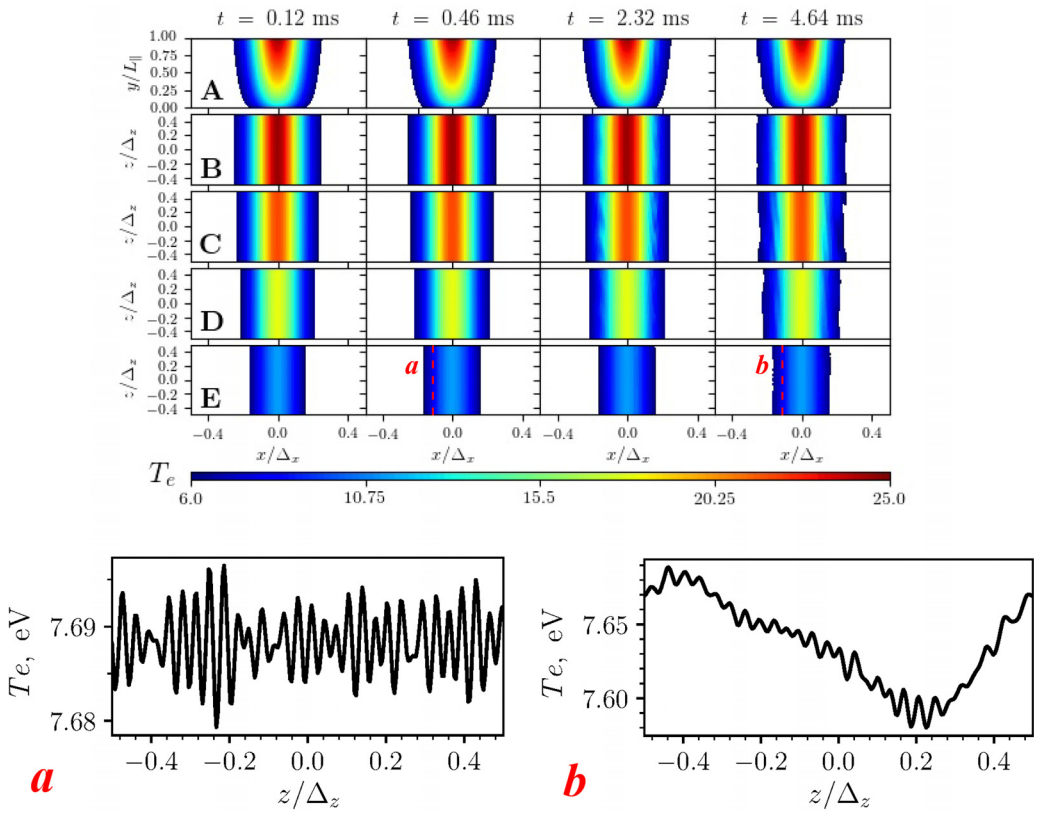

FIG. 4. CCI driven dynamics of the electron temperature in various domain cross sections obtained in the case with $\max(T_u) = 25$ eV. Slice A is taken at $z = 0.5\Delta_z$, and slices B-E are taken at $y = L_\parallel, (2/3)L_\parallel, (1/3)L_\parallel, 0$. Panels (a) and (b) show the distributions of the electron temperature in the z direction at positions, marked with the red lines, in the linear (a) and saturated (b) phases of the instability.

showing that saturated turbulence becomes dominated by large-scale structures with toroidal wavelengths on the order of Δ_ζ. The obtained spatial spectra of current-convective turbulence also qualitatively agree with data on CCI dynamics, recently shown in Ref. 24.

It is worth mentioning that spatial spectra of the T_e fluctuations in the near target region obtained for other values of the upstream electron temperature (see Fig. 6) also demonstrate the similar behavior of turbulence, viz., transition from small- to large-scale oscillations in the toroidal direction. Herein, regions of turbulent activity remain practically in the same positions, as in the case shown in Fig. 5, panel (b).

Temporal spectra of the saturated parallel current and electron temperature fluctuations, obtained in the case with $\max(T_u) = 25$ eV, are presented in Figs. 7 and 8.

As seen in Fig. 7, the spectrum of the signal $\delta j_\parallel(t)$ at the ISP is dominated by a single mode with the frequency of $f \approx 6$ kHz. In contrast to the previous modeling results,[24] which have shown the

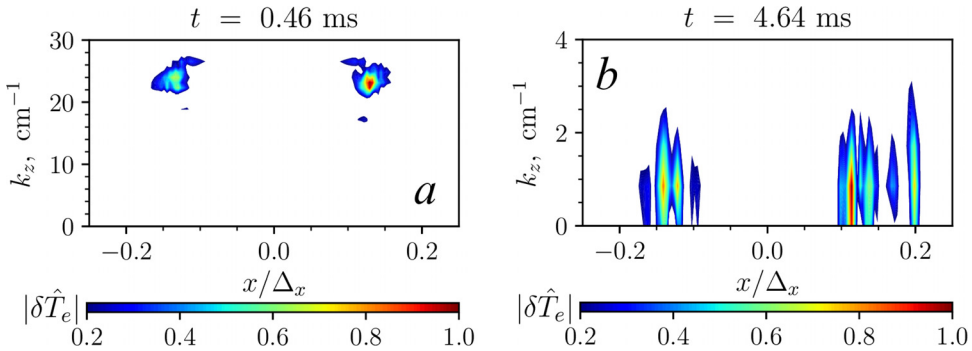

FIG. 5. Spatial spectra of T_e fluctuations near the target plate during the linear stage of the CCI (a) and for saturated turbulence (b), found in the modeling case with $\max(T_u) = 25$ eV.

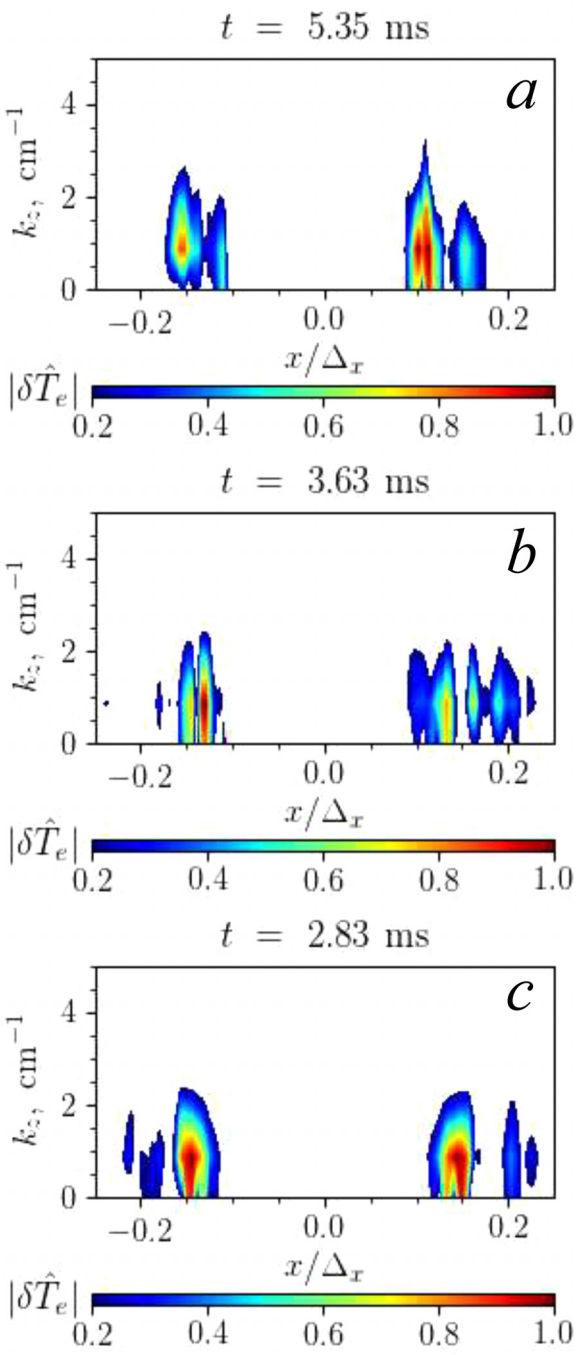

FIG. 6. Spatial spectra of T_e fluctuations found in the near target region in the modeling cases with $\max(T_u) = 15, 35, 65$ eV, panels (a)–(c), respectively.

coexistence of strong modes in spectra of the parallel current oscillations, the spectrum now has only one strong component. Its frequency, nevertheless, remains very close to the experimental values $f_{exp} \sim 5$ kHz. The amplitude of the fluctuations in the demonstrated case is estimated at the level $S[\delta j_\parallel] \approx 2.1\,\mathrm{A}\cdot\mathrm{cm}^{-2}$ ($S[F]$ is the

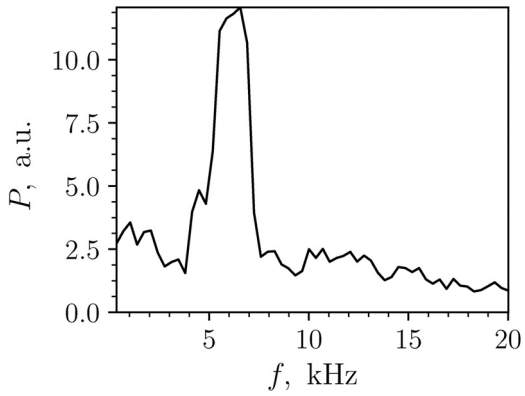

FIG. 7. Frequency spectra of saturated parallel current fluctuations measured at the inner strike point in the modeling case with $\max(T_u) = 25$ eV.

standard deviation of the signal F), which is well below the background value of the plasma current $\mathbb{E}[j_\parallel] = 26.1\,\mathrm{A}\cdot\mathrm{cm}^{-2}$. This result agrees with the conclusion on the smallness of amplitudes of saturated fluctuations, driven by the CCI within its basic physical model, incorporating only the minimum set of mechanisms required to start/suppress the instability.[23,24]

Figure 8 demonstrates the frequency spectra of the electron temperature fluctuations found at the fixed points No. 1–3 across the simulation domain. Similar to the modeling case with the magnetic geometry with a different set of parameters,[24] the current-convective

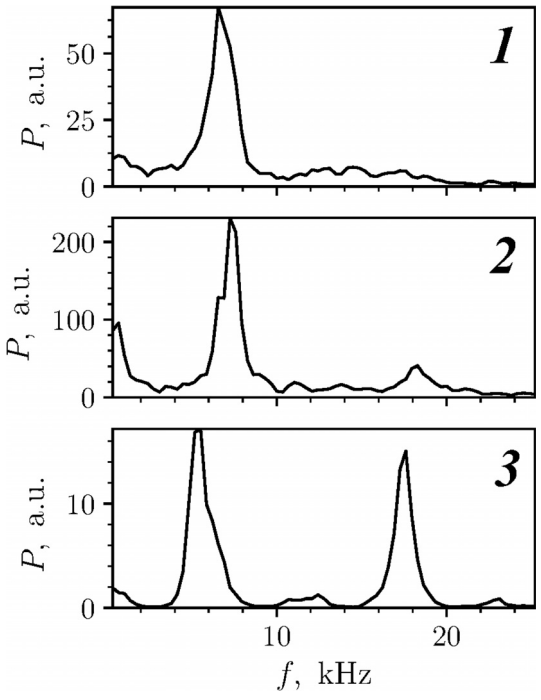

FIG. 8. Frequency spectra of saturated electron temperature fluctuations measured at the fixed points 1–3 in the modeling case with $\max(T_u) = 25$ eV.

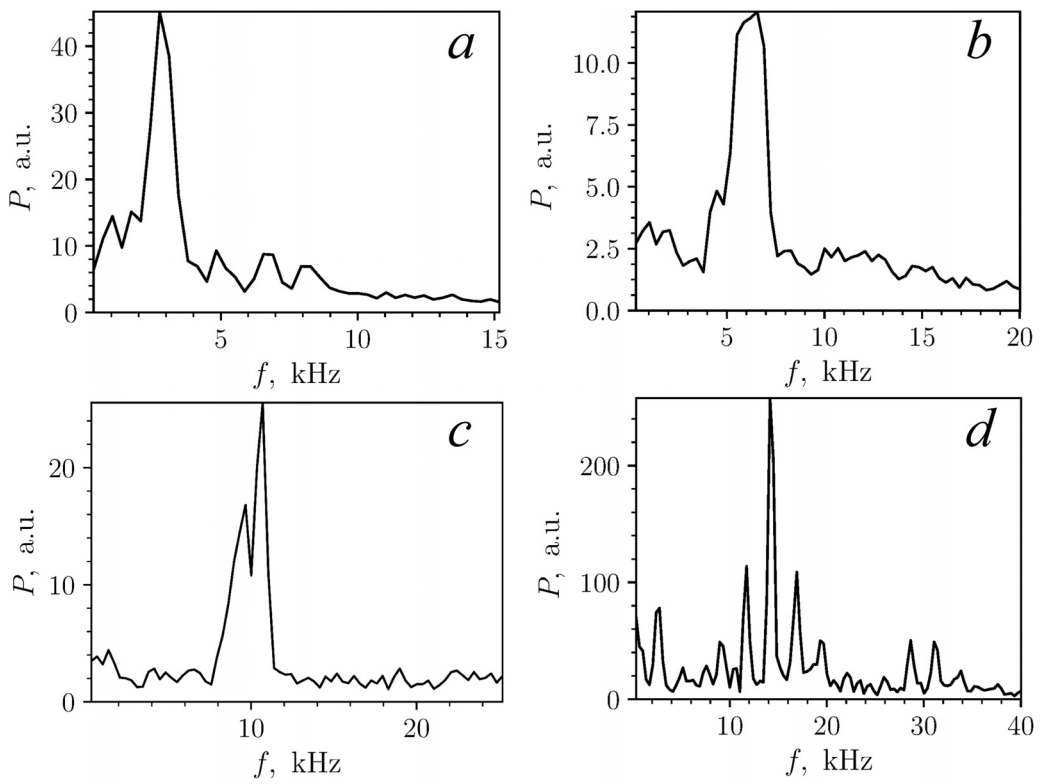

FIG. 9. Frequency spectra of parallel current fluctuations found in cases with $\max(T_u) = 15, 25, 35, 65$ eV, panels (a)–(d), respectively.

turbulence is also dominated by low-f components; herein, in the near-target region (the fixed point No. 3), another strong component with $f \approx 17$ kHz also appears. The found spectra qualitatively comply with those obtained in Ref. 24; however, the frequencies of the dominant modes, found in two simulation cases, differ from each other by a factor 2–3. In the present case, $f \sim 6$ kHz, whereas in the modeling case with $\max(T_u) = 25$ eV considered in Ref. 24, the dominant modes had frequencies of $f \sim 12 - 16$ kHz. This behavior is most likely attributed to the different geometries of plasma and magnetic fields employed for two modelings [recall that both the transverse scale of the variation of the electrical conductivity and the magnitude of the parallel electric field (depending on the connection length $L_\parallel$) drive the CCI]. For this reason, further scans of the CCT characteristics on the geometric parameters of plasma and the magnetic field will be performed.

The amplitudes of the T_e fluctuations measured at the fixed points 1–3 are small compared to the background values of the electron temperature. The mean values of T_e and standard deviations of

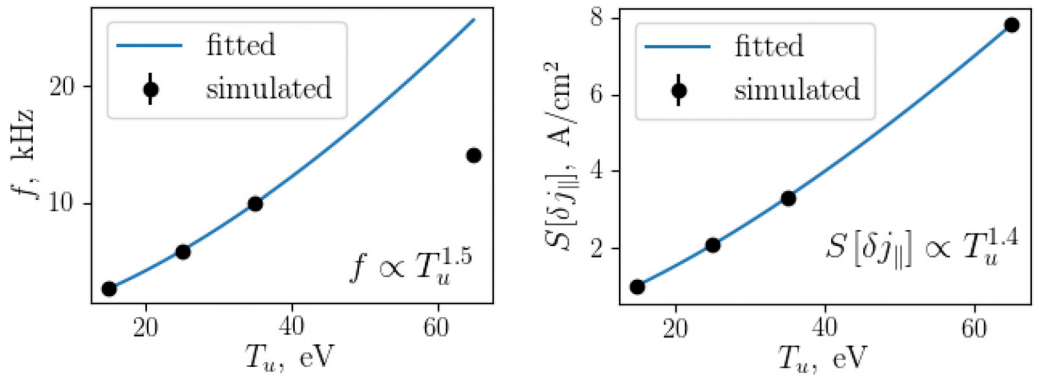

FIG. 10. Numerical fits for the frequency of the dominant mode and for the amplitude of $j_\parallel$ fluctuations at the ISP, based on data in Table II. For brevity, $\max(T_u)$ is shortened to T_u. Note that the fit for the frequency of the dominant mode is based only on those values of T_u, which comply with the experimental data.

the signals δT_e at the reference points 1–3 are estimated to be $\mathbb{E}[T_e] = 14.50, 13.61, 13.33\,\text{eV}$ and $S[\delta T_e] = 0.04, 0.42, 0.14\,\text{eV}$, respectively. The small values of ratios $S[\delta T_e]/\mathbb{E}[T_e]$ are somewhat comparable to those found in previous simulations[24] and comply with the above conclusion that within the basic set of physical mechanisms determining the CCI dynamics, the instability cannot sustain strong variations of plasma parameters observed in experiments. Discussion of the way to improve the situation will be given further on in Sec. V.

C. Dependence of turbulence characteristics on parameters of background plasma

To assess the dependence of the characteristics of the current-convective turbulence (the amplitudes of oscillations and frequencies of the dominant modes) on the parameters of background plasma, we have performed several parameter scans. The parameters chosen for this purpose were the upstream electron temperature and plasma density, as they govern dynamics of the CCI within the employed physical model of the instability.

1. Electron temperature scan

To estimate the impact of the maximum upstream electron temperature on the turbulence parameters, we have analyzed the parallel current fluctuations at the inner strike point. Four different values of $\max(T_u)$ were selected: 15, 25, 35, and 65 eV. The first three values of the temperature approximately correspond to those measured in experiments,[21,30] whereas the fourth one, although incompatible with the experimental data, was chosen to test the turbulence characteristics in the large temperature region.

The obtained frequency spectra of $\delta j_\parallel$ are shown in Fig. 9. Standard deviations of the fluctuations, mean background values of the parallel current, and the frequencies of the dominant modes in spectra are summarized in Table II.

It can be seen from the demonstrated data that the increase in the upstream electron temperature leads to the growth of the frequencies and amplitudes of the dominant modes. The increase in the mode amplitudes, however, is surpassed by that of the mean values of the parallel current. For example, in the "cold" plasma case $[\max(T_u) = 15\,\text{eV}]$, the fluctuation level for the $j_\parallel$ signal is $S[\delta j_\parallel]/\mathbb{E}[j_\parallel] \approx 0.11$, whereas for the "hot" plasma case $(\max(T_u) = 65\,\text{eV})$, the very same ratio is $S[\delta j_\parallel]/\mathbb{E}[j_\parallel] \approx 0.03$. Thus, although leading to a more intense turbulent activity, the increase in the overall temperature of plasma has the diminishing impact on its dynamics, as it becomes practically unaffected by the onset of the current-convective turbulence.

TABLE III. Parameters of the parallel current fluctuations, measured at the inner strike point, for the plasma density scan.

n_0, $10^{19} \times \text{m}^{-3}$	f, kHz[a]	$S[\delta j_\parallel]$, A/cm^2	$\mathbb{E}[j_\parallel]$, A/cm^2
4.8	9.7	2.5	54.9
5.4	10.0	3.3	54.9
6.0	9.0	4.2	54.9

[a]The frequency of the dominant mode was found as the center-of-mass of the power spectrum with values below the threshold level, $P/P_{\max} < 0.4$, set to zero.

The scalings of the amplitudes and frequencies of current fluctuations on the maximum upstream electron temperature in the range of $\max(T_u) = 15 - 35\,\text{eV}$ can be summarized as follows:

$$f \propto [\max(T_u)]^{1.5}, \quad S[\delta j_\parallel] \propto [\max(T_u)]^{1.4}. \tag{11}$$

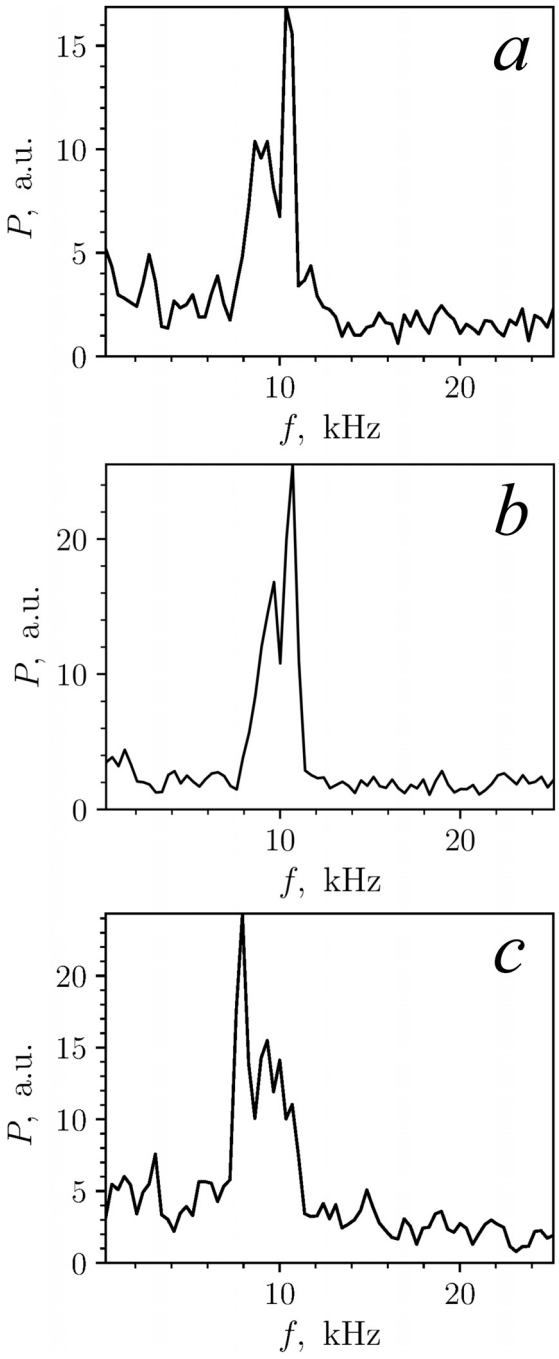

FIG. 11. Frequency spectra of parallel current fluctuations, found in the modeling case with $\max(T_u) = 35\,\text{eV}$ and $n_0 = 4.8 \times 10^{19}\,\text{m}^{-3}$ (a), $n_0 = 5.4 \times 10^{19}\,\text{m}^{-3}$ (b), and $n_0 = 6.0 \times 10^{19}\,\text{m}^{-3}$ (c).

In the "high" temperature range, $\max(T_u) > 35$ eV, the slope of the dependency $f(T_u)$ becomes shallower, as the instability damping mechanism due to the parallel electron thermal conductivity starts playing a stronger role in determining plasma dynamics, compared to the cases with lower electron temperatures. Figure 10 demonstrates the numerical fits of the turbulence parameters based on data in Table II.

2. Plasma density scan

To elucidate the impact of the plasma density on turbulence parameters, we also chose to analyze the parallel current fluctuations at the inner strike point. For the scan, we have fixed the upstream electron temperature at the level $\max(T_u) = 35$ eV and varied the density $n_0 = \{4.8; 5.4; 6.0\} \times 10^{19}\ \mathrm{m}^{-3}$ in the range relevant to the experimental observations.[21] The results of simulations are shown in figures and also covered in Table III.

From the demonstrated data (Fig. 11, Table III), it can be seen that the frequency of the dominant component in each spectra varies weakly and remains in the range, $f \sim 10$ kHz; herein, the amplitudes of current perturbations increase. This is an expected result since in the present CCI model, the plasma density influences the instability dynamics primarily through the electron thermal conductivity damping mechanism. The increase in the plasma density reduces the parallel electron temperature diffusivity, $2\varkappa_{e\|}/(3n_0)$, and thus leads to the growth of the fluctuations level.

The numerical fits for the CCT parameters (the frequency of the dominant mode and deviations of current fluctuations) are shown in Fig. 12. The found power-law dependencies of the turbulence parameters on the plasma density can be expressed as

$$f \propto n_0^{-0.3}, \quad S[\delta j_\|] \propto n_0^{2.3}. \tag{12}$$

V. DISCUSSION AND CONCLUSIONS

We have performed simulations of the current-convective turbulence within the DIII-D-like detached divertor conditions. For modeling, the basic physical model of the instability, incorporating only the minimum set of components necessary to start/damp the instability, was used. Nevertheless, even within this initial model, we have been able to reproduce several important turbulence features analogous to those found in experiments.

For the magnetic field geometry and the set of plasma parameters (the transverse decay length of the profiles, the upstream electron temperature, and the background plasma density) similar to those of the DIII-D, we have shown that the frequency and spatial spectra of the current oscillations at the divertor plates demonstrate the behavior, which is also similar to both the experiments[21] and previous simulations.[24] The frequency spectra showed the dominance of the low-f modes, with frequencies on the order $f \sim 1 - 10$ kHz, which reasonably agree with the experimental values. As in the previous modeling case,[24] the spatial spectra of turbulence also showed the transition from the small-scale fluctuations in the toroidal direction to the large-scale ones, characterized by the mode numbers $n_\zeta \sim 1, 2$. The dominance of the low-n modes in spatial spectra of saturated turbulence was also found in experiments.[21]

A series of parameter scans were performed to analyze the response of the turbulence characteristics (such as the amplitude of current fluctuations at the inner strike point and frequencies of the dominant mode) to the changes in the background plasma parameters. The simulations have shown the results that could have been qualitatively anticipated prior to modeling. The increase in the upstream electron temperature (and, as a result, in the overall electron temperature in the whole modeling domain) yielded the increase in both the amplitudes and the frequencies of the fluctuations. However, in the case of the plasma current, this increase was completely overshadowed by the growth of the equilibrium values of the current so that the relative effect of the CCI driven oscillations on the background profiles was diminished. This could be attributed to the interplay between the CCI driving and damping mechanisms,[22] with the intensity of the latter growing rapidly with the increase in the electron temperature (recall that the parallel electron thermal conductivity $\varkappa_{e\|} \propto T_e^{5/2}$). As for the impact of the plasma density on turbulence parameters, our simulations have revealed that it has a weak impact (within the employed model) on the frequencies of the dominant turbulence modes, whereas the amplitude of fluctuations increased. This is in agreement with the fact that the increase in the plasma density reduces the parallel electron temperature diffusivity, thus reducing the effectiveness of the CCI damping mechanism.

The major discrepancy between the obtained results and the experimental observations is related to the smallness of the fluctuation amplitudes with respect to the background values of the corresponding

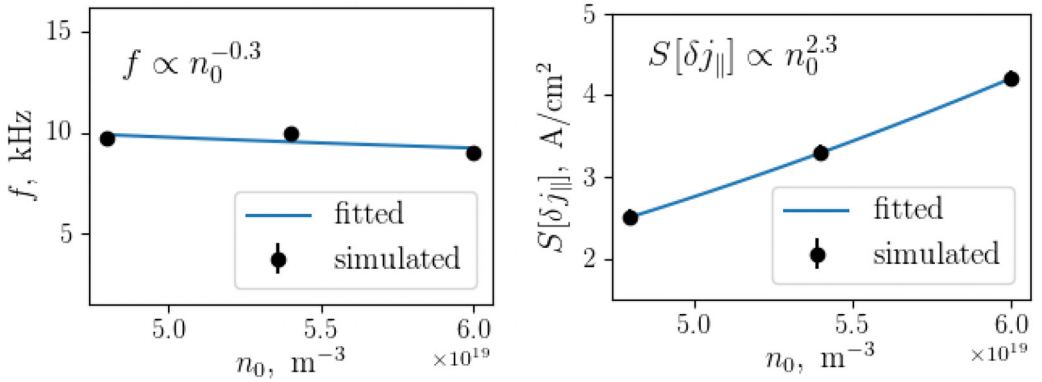

FIG. 12. Numerical fits for the frequency of the dominant mode and for the amplitude of $j_\|$ fluctuations at the ISP, based on data in Table III.

plasma profiles. For example, in the case of the electron temperature disturbances, their amplitude did not exceed $S[\delta T_e] \sim 0.5$ eV, which is well below the background values of the electron temperature $T_e \sim 10$ eV. This conclusion had already been drawn in the previous studies.[23,24] The possible solution to the problem is the incorporation of the additional physical mechanisms into the CCI physical model, such as the parallel convection. The first simulations with these components turned on[31] have already demonstrated that this could amend the mentioned problem.

In the long run, the CCI model has to be enriched with new physical mechanisms to make it more relevant to the conditions of the divertor region of a real machine. The first priority components are the parallel plasma convection and the curvature of the magnetic field lines. These issues will be addressed in future publications.

ACKNOWLEDGMENTS

A. A. Stepanenko would like to acknowledge the financial support of the theoretical work, presented in this paper, under Grant No. 18-12-00329 from the Russian Science Foundation. H. Q. Wang would like to thank for the financial support of the experimental work at the DIII-D tokamak from the U.S. Department of Energy under Award No. DE-FC02-04ER54698. S. I. Krasheninnikov would like to acknowledge the financial support from the U.S. Department of Energy under Award No. DE-FG02-04ER54739 at UCSD, which allowed supervising the ongoing research on the problem.

REFERENCES

[1]A. Loarte, R. Monk, J. Martin-Solis, D. Campbell, A. Chankin, S. Clement, S. Davies, J. Ehrenberg, S. Erents, H. Guo *et al.*, Nucl. Fusion **38**, 331 (1998).
[2]A. Loarte, B. Lipschultz, and A. Kukushkin, Nucl. Fusion **47**, S203 (2007).
[3]R. Pitts, S. Carpentier, F. Escourbiac, T. Hirai, V. Komarov, S. Lisgo, A. Kukushkin, A. Loarte, M. Merola, A. S. Naik *et al.*, J. Nucl. Mater. **438**, S48 (2013).
[4]S. Krasheninnikov, A. Kukushkin, and A. Pshenov, Phys. Plasmas **23**, 055602 (2016).
[5]S. Krasheninnikov and A. Kukushkin, J. Plasma Phys. **83**, 155830501 (2017).
[6]A. Pshenov, A. Kukushkin, and S. Krasheninnikov, Phys. Plasmas **24**, 072508 (2017).
[7]A. Kukushkin and S. Krasheninnikov, Plasma Phys. Controlled Fusion **61**, 074001 (2019).
[8]X. Xu and R. Cohen, Contrib. Plasma Phys. **36**, 202 (1996).
[9]B. Chen, X. Xu, T. Xia, M. Porkolab, E. Edlund, B. LaBombard, J. Terry, J. Hughes, S. Mao, M. Ye *et al.*, Nucl. Fusion **57**, 116025 (2017).
[10]I. Garcia-Cortes, C. Hidalgo, S. Ali-Arshad, S. Clement, S. Davies, J. Lingertat, A. Loarte, G. Matthews, R. Monk *et al.*, Plasma Phys. Controlled Fusion **38**, 2051 (1996).
[11]R. Moyer, J. Cuthbertson, T. Evans, G. Porter, and J. Watkins, J. Nucl. Mater. **241**, 633 (1997).
[12]A. Hatayama, H. Segawa, R. Schneider, D. Coster, N. Hayashi, S. Sakurai, N. Asakura, and M. Ogasawara, Nucl. Fusion **40**, 2009 (2000).
[13]N. Ohno, K. Furuta, and S. Takamura, J. Plasma Fusion Res. **80**, 275 (2004).
[14]H. Guo, X. Gao, J. Li, G.-N. Luo, S. Zhu, J. Chang, Y. Chen, W. Gao, X. Gong, Q. Hu *et al.*, J. Nucl. Mater. **415**, S369 (2011).
[15]S. Potzel, M. Wischmeier, M. Bernert, R. Dux, H. Müller, A. Scarabosio, and the ASDEX Upgrade Team, Nucl. Fusion **54**, 013001 (2014).
[16]A. Leonard, Plasma Phys. Controlled Fusion **60**, 044001 (2018).
[17]I. Hutchinson, Nucl. Fusion **34**, 1337 (1994).
[18]S. Krasheninnikov, Phys. Plasmas **4**, 3741 (1997).
[19]S. Krasheninnikov, M. Rensink, T. Rognlien, A. Kukushkin, J. Goetz, B. LaBombard, B. Lipschultz, J. Terry, and M. Umansky, J. Nucl. Mater. **266–269**, 251 (1999).
[20]R. Smirnov, A. Kukushkin, S. Krasheninnikov, A. Y. Pigarov, and T. Rognlien, Phys. Plasmas **23**, 012503 (2016).
[21]H. Wang, J. Watkins, H. Guo, A. Leonard, D. Thomas, A. Stepanenko, S. Krasheninnikov, and J. Boedo, "Enhanced particle flux due to localized divertor MHD instability in DIII-D tokamak," Phys. Plasmas (in press).
[22]S. Krasheninnikov and A. Smolyakov, Phys. Plasmas **23**, 092505 (2016).
[23]A. Stepanenko and S. Krasheninnikov, Phys. Plasmas **25**, 012305 (2018).
[24]A. Stepanenko and H. Q. Wang, Plasma Phys. Rep. **45**, 627 (2019).
[25]X. Xu, R. Cohen, T. Rognlien, and J. Myra, Phys. Plasmas **7**, 1951 (2000).
[26]A. Dimits, Phys. Rev. E **48**, 4070 (1993).
[27]W. D. D'haeseleer, W. N. Hitchon, J. D. Callen, and J. L. Shohet, *Flux Coordinates and Magnetic Field Structure: A Guide to a Fundamental Tool of Plasma Theory* (Springer Science & Business Media, 2012).
[28]B. Dudson, M. Umansky, X. Xu, P. Snyder, and H. Wilson, Comput. Phys. Commun. **180**, 1467 (2009).
[29]A. C. Hindmarsh, P. N. Brown, K. E. Grant, S. L. Lee, R. Serban, D. E. Shumaker, and C. S. Woodward, ACM Trans. Math. Software **31**, 363 (2005).
[30]J. Boedo, A. McLean, D. Rudakov, and J. Watkins, Plasma Phys. Controlled Fusion **60**, 044008 (2018).
[31]A. Stepanenko, H. Wang, and S. Krasheninnikov, in APS Meeting Abstracts (2018).